

Fine structure of K-excitons in multilayers of transition metal dichalcogenides

A. O. Slobodeniuk,^{1,*} L. Bala,^{1,2} M. Koperski,^{1,3,4} M. R. Molas,^{1,2} P. Kossacki,²
K. Nogajewski,^{1,2} M. Bartos,¹ K. Watanabe,⁵ T. Taniguchi,⁵ C. Faugeras,¹ and M. Potemski^{1,2,†}

¹*Laboratoire National des Champs Magnétiques Intenses,
CNRS-UGA-UPS-INSA-EMFL, 25 avenue des Martyrs, 38042 Grenoble, France*

²*Institute of Experimental Physics, Faculty of Physics,
University of Warsaw, ul. Pasteura 5, 02-093 Warszawa, Poland*

³*School of Physics and Astronomy, University of Manchester, Oxford Road, Manchester, M13 9PL, UK*

⁴*National Graphene Institute, University of Manchester, Oxford Road, Manchester, M13 9PL, UK*

⁵*National Institute for Materials Science, 1-1 Namiki, Tsukuba 305-0044, Japan*

Reflectance and magneto-reflectance experiments together with theoretical modelling based on the $\mathbf{k} \cdot \mathbf{p}$ approach have been employed to study the evolution of direct bandgap excitons in MoS₂ layers with a thickness ranging from mono- to trilayer. The extra excitonic resonances observed in MoS₂ multilayers emerge as a result of the hybridization of Bloch states of each sub-layer due to the interlayer coupling. The properties of such excitons in bi- and trilayers are classified by the symmetry of corresponding crystals. The inter- and intralayer character of the reported excitonic resonances is fingerprinted with the magneto-optical measurements: the excitonic g -factors of opposite sign and of different amplitude are revealed for these two types of resonances. The parameters describing the strength of the spin-orbit interaction are estimated for bi- and trilayer MoS₂.

I. INTRODUCTION

Scientific curiosity to uncover the properties of new materials and to demonstrate their possible novel functionalities drive the research efforts focused on atomically-thin matter, and, in particular, on thin layers of semiconducting transition metal dichalcogenides (S-TMD)[1–4]. Intense works have been devoted to studies of S-TMD monolayers which appeared to be the efficient light emitters, the two-dimensional semiconductors with a direct bandgap positioned at the K^\pm points of their 1-st hexagonal Brillouin zone (BZ) [5–7]. New and rich possibilities of tuning the band structure, the strength of Coulomb interaction, and thus the optical properties, are opened when stacking the S-TMD monolayers into a form of multilayers and/or hetero-layers [8–16]. The properties of the archetypes of S-TMD stacks which are the thermodynamically stable 2H-stacked multilayers are to be well understood first.

In 2H stacks of N monolayers (NML), the electronic bands are known to be effectively modified, with N , in the range outside the K^\pm points of the BZ [17–23]. This, in particular, implies the indirect bandgap in NMLs when $N > 1$, what strongly affects the emission spectra of these multilayers [24–29]. Instead, more subtle effects of the hybridization of electronic states around the direct bandgap which appears at K^\pm points of the BZ in any NML are relevant for the absorption-type processes [30–32]. Understanding the absorption response of S-TMD multilayers might be of special importance for their potential applications in photo-sensing or photo-voltaic devices [33–36].

In this paper we present the theoretical outline (based on $\mathbf{k} \cdot \mathbf{p}$ approach [17, 27, 30, 37]) and the experimental data (results of reflectance and magneto-reflectance measurements), which, in a consistent manner, unveil the nature of direct bandgap (K^\pm points) excitonic transitions in 2H-stacked S-TMDs multilayers. The geometry of 2H stacking, wherein each subsequent layer is 180° rotated around previous one, induces interaction and hybridization of the Bloch states in $K^+/K^-/K^+ \dots (K^-/K^+/K^- \dots)$ points of subsequent monolayers, which form the $K^+(K^-)$ valleys of the multilayer. Such non-trivial interlayer coupling delocalizes the electron states in the out-of-plane direction, which leads to the formation of the new type of excitons, associated with K^\pm valleys of multilayers as well as bulk crystals [27, 38, 39]. We classify such excitons, associate them with the symmetry of the crystal and describe their properties in terms of the simple theoretical model. Notably, the intra- or interlayer character of the excitonic transitions is fingerprinted with, correspondingly, positive or negative sign of the g -factor associated to these transitions.

Due to the different symmetries of the conduction and valence band orbitals, the hybridization of K^\pm -electronic states in NML occurs predominantly in the valence band and is more effective when the spin-orbit splitting Δ_v in the valence band is small. MoS₂ crystals, with the smallest Δ_v among all other S-TMDs, have been therefore chosen for the investigations. In the experiments, we have largely profited of the significantly improved optical quality of MoS₂ layers when they are encapsulated in between the hexagonal boron nitride (hBN)[11, 40–44]. We consider the bi- and trilayer systems as the simplest multilayer representatives with different spatial symmetry. Comparing the experimental data with the theoretical expectation on a more quantitative level, we discuss the characteristic parameters which reflect the effects of

* artur.slobodeniuk@lncmi.cnrs.fr

† marek.potemski@lncmi.cnrs.fr

spin-orbit interaction in our bi- and tri-layer MoS₂. Intriguingly, we estimate/speculate that in these multilayers the spin-orbit splitting in the conduction band is quite large (~ 50 meV) whereas the spin-orbit coupling parameter for the valence band ($\sim 120\text{--}140$ meV) is somewhat small, as compared to the expected values for the MoS₂ monolayer.

The paper is organized as follows. The section II introduces the theoretical description of the interlayer coupling and optically active transitions in 2H stacked multilayers. In the section III we present the experimental data for excitonic resonances in bi- and trilayer of MoS₂. In the section IV we outline the properties of multilayers and the possible applications of such materials. In the Appendix A the samples, instrumentation and experimental details are presented. The Appendices B and C contain the derivation and discussion of the exciton g -factors in bi- and trilayer of MoS₂ respectively.

II. THEORETICAL DESCRIPTION

We consider the optically active transitions at the K^\pm points in 2H-stacked multilayer S-TMD crystals encapsulated in hBN. Our investigation is based on $\mathbf{k} \cdot \mathbf{p}$ approximation. We focus on the optical properties of such crystals at K^+ point for brevity [27]. The results for K^- point can be obtained by analogy.

We briefly remind the features of S-TMD *monolayer* which will be used in the subsequent description of the multilayer structures. Namely, a single layer crystal is a direct band gap semiconductor. The maximum of valence (VB) and minimum of conduction (CB) bands are located at the K^\pm points of BZ. Due to strong spin-orbit interaction both bands are spin-split (from hundreds of meV in VB, up to tens meV in CB). Hence, Bloch states in the corresponding points can be presented as a tensor product of spin and spinless states. The spinless valence $|\Psi_v\rangle$ and conduction $|\Psi_c\rangle$ band states at the K^+ point are made predominantly from $d_{x^2-y^2} + id_{xy}$ and d_{z^2} orbitals of transition metal atoms respectively [45, 46]. Due to time-reversal symmetry (TRS) the analogous states at the K^- point are complex conjugated to the previous ones, *i.e.* they are made from $d_{x^2-y^2} - id_{xy}$ and d_{z^2} orbitals accordingly. The TRS also dictates that Bloch states with the same band index (c or v) but with opposite spins in different valleys have equal energies. The crystal spatial symmetry together with TRS define the optical properties of monolayers — only σ^\pm polarized light can be absorbed or emitted at the K^\pm points respectively. Since the VB and CB are split, there are two possible optical transitions (which conserve spin) at the K^\pm points — the lower-energy T_A and the higher-energy T_B ones. All the described features are depicted on Fig. 1 for the case of MoS₂.

A *bilayer* crystal can be presented as two monolayers separated by a distance $l \sim 6$ Å [47], and in which the top layer is rotated with respect to the bottom one by

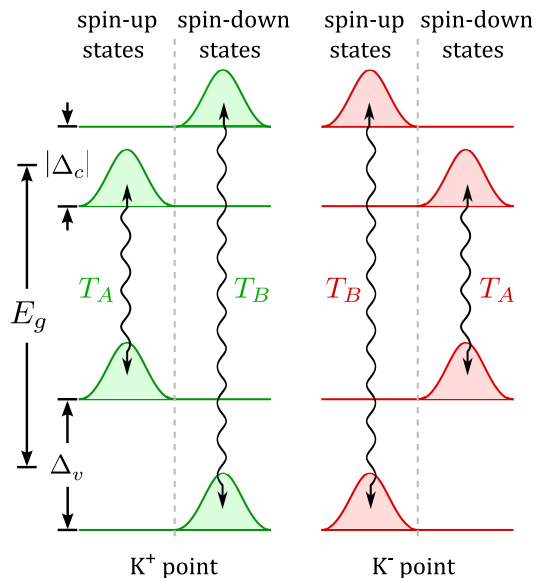


FIG. 1. Sketch of band positions and optical transitions at the K^+ and K^- points of the Brillouin zone in a monolayer of MoS₂. Green and red bump structures represent conduction and valence band states associated with transitions active correspondingly in the σ^+ and σ^- polarizations. Solid wavy arrows denote all possible (T_A and T_B) optical transitions. $|\Delta_c|$ and Δ_v define the absolute values of spin-orbit splitting in the CB and VB, respectively. E_g is the single-particle band gap.

180° . We arrange them in $z = l/2$ and $z = -l/2$ planes, respectively (see Fig. 2). In this presentation, the crystal possesses the centrosymmetry I with an inversion center in the $z = 0$ plane. The bilayer embedded in between two flakes of the same material (in our case, hBN), thickness and size conserves this symmetry. Therefore, one can extend the $\mathbf{k} \cdot \mathbf{p}$ model proposed in [30] also for this case.

Let us examine the Bloch states of the valence and conduction bands at the K^+ point of bilayer. We construct them from the Bloch states of top and bottom layers considering them separately. Namely, we introduce the states $|\Psi_n^{(m)}\rangle \otimes |s\rangle$, where $m = 1, 2$ is a layer index (for bottom and top layers, respectively), $n = v, c$ is a band index (for VB and CB) and $s = \uparrow, \downarrow$ specifies spin degree of freedom. The bottom (first) layer states $|\Psi_v^{(1)}\rangle$ and $|\Psi_c^{(1)}\rangle$ are made predominantly from $d_{x^2-y^2} + id_{xy}$ and d_{z^2} orbitals of transition metal atoms respectively [45, 46]. They coincide with monolayer spinless states $|\Psi_v\rangle$ and $|\Psi_c\rangle$ mentioned before. The top (second) layer states $|\Psi_v^{(2)}\rangle$ and $|\Psi_c^{(2)}\rangle$ are made from $d_{x^2-y^2} - id_{xy}$ and d_{z^2} orbitals and coincide with spinless states at the K^- point of monolayer. The top and bottom states are connected by the relation $|\Psi_n^{(2)}\rangle = K_0 I |\Psi_n^{(1)}\rangle$, where K_0 and I are the complex conjugation and central inversion operators respectively. Finally, we suppose the orthogonality of the basis states from different layers and bands

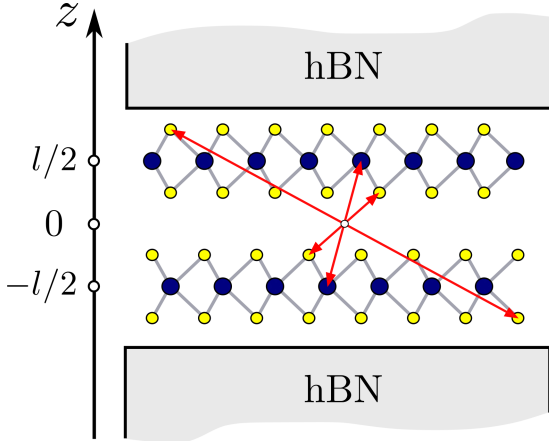


FIG. 2. The bilayer crystal embedded in between two thick hBN flakes, side view. The origin of all red arrows represents the inversion center of the crystal. The arrows, which lay on the same line, depict the inversion symmetry of the crystal. Namely, the tips of the corresponding arrows indicate the pair of atoms, which positions transform into each other after inversion procedure.

$$\langle \Psi_n^{(m)} | \Psi_{n'}^{(m')} \rangle = \delta_{nn'} \delta_{mm'}.$$

The initial basis states in a given layer are affected by crystal fields of another layer and surrounding hBN medium. Such fields being considered as a perturbation in $\mathbf{k} \cdot \mathbf{p}$ model produce intra- and interlayer corrections to the bilayer Hamiltonian. Namely, the intralayer ones renormalize the band gap E_g and spin-splittings Δ_c, Δ_v for the electron excitations in the considered layer. Due to the symmetry of the system, the parameters of the other layer get the same modifications. The interlayer corrections link the states from different layers. The symmetry analysis of such terms demonstrates *i)* the strong coupling between VB basis states with the same spins; *ii)* the quasi-momentum dependent coupling between CB basis states with the same spins; *iii)* the coupling between VB and CB basis states of the opposite spins, which appears due to spin-orbit interaction. The latter term is supposed to be small and is omitted from our study. In this case, the spin-up and spin-down states of bilayer are decoupled and can be considered separately.

As a result, the VB Hamiltonian written in the basis $\{|\Psi_v^{(1)}\rangle \otimes |s\rangle, |\Psi_v^{(2)}\rangle \otimes |s\rangle\}$ takes the form

$$H_{vs}^{(2)} = \begin{bmatrix} \sigma_s \frac{\Delta_v}{2} & t \\ t & -\sigma_s \frac{\Delta_v}{2} \end{bmatrix}, \quad (1)$$

where $\sigma_s = +1(-1)$ for $s = \uparrow(\downarrow)$. The parameter $t \sim 40-70$ meV [30] defines the coupling between valence bands from different layers. The CB Hamiltonian, written in the basis $\{|\Psi_c^{(1)}\rangle \otimes |s\rangle, |\Psi_c^{(2)}\rangle \otimes |s\rangle\}$ is

$$H_{cs}^{(2)} = \begin{bmatrix} E_g + \sigma_s \frac{\Delta_c}{2} & uk_+ \\ uk_- & E_g - \sigma_s \frac{\Delta_c}{2} \end{bmatrix}, \quad (2)$$

where E_g is the band gap of bilayer and $k_{\pm} = k_x \pm ik_y$. Both Hamiltonians are written up to $O(k^2)$.

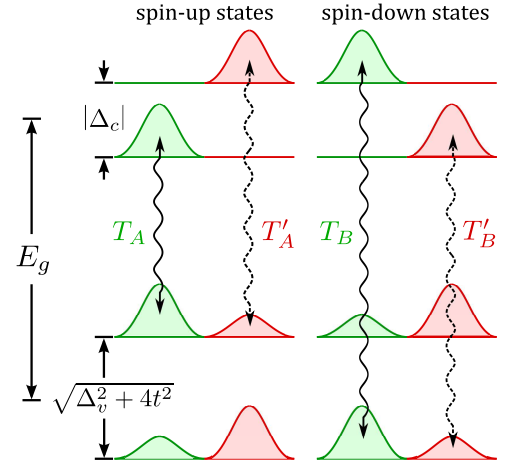


FIG. 3. Sketch of the bands positions and optical transitions at the K^+ of the BZ in a bilayer of MoS_2 . Green and red bump structures represent conduction and valence band states associated with transitions active in the σ^+ and σ^- polarizations respectively. Solid (dashed) wavy arrows denote optical transitions due to the intralayer (interlayer) A and B excitons. $|\Delta_c|$ and $\sqrt{\Delta_v^2 + 4t^2}$ denote the splitting in the CB and VB, respectively. E_g is the single particle band gap.

The bilayer VB have the energies $E_v^{\pm} = \pm \sqrt{\Delta_v^2/4 + t^2}$. The corresponding upper-energy eigenstates are

$$\begin{aligned} |\Phi_{v\uparrow}^+\rangle &= \left[\cos\theta |\Psi_v^{(1)}\rangle + \sin\theta |\Psi_v^{(2)}\rangle \right] \otimes |\uparrow\rangle, \\ |\Phi_{v\downarrow}^+\rangle &= \left[\sin\theta |\Psi_v^{(1)}\rangle + \cos\theta |\Psi_v^{(2)}\rangle \right] \otimes |\downarrow\rangle, \end{aligned} \quad (3)$$

where we introduced $\cos(2\theta) = \Delta_v / \sqrt{\Delta_v^2 + 4t^2}$. The low-energy eigenstates $|\Phi_{v\uparrow}^-\rangle$ and $|\Phi_{v\downarrow}^-\rangle$ can be derived from the first ones by replacing $\cos\theta \rightarrow -\sin\theta, \sin\theta \rightarrow \cos\theta$. The new VB are doubly degenerated by spin.

The CB states do not interact with each other in K^+ valley (*i.e.* in $k_x, k_y \rightarrow 0$ limit). Hence, in leading order they are not mixed and form doubly degenerated bands with energies $E_g \pm \Delta_c/2$. In further we focus on MoS_2 bilayer with $\Delta_c < 0$. For this case, the upper and lower energy CB states are $\{|\Psi_c^{(1)}\rangle \otimes |\downarrow\rangle, |\Psi_c^{(2)}\rangle \otimes |\uparrow\rangle\}$ and $\{|\Psi_c^{(1)}\rangle \otimes |\uparrow\rangle, |\Psi_c^{(2)}\rangle \otimes |\downarrow\rangle\}$, respectively.

All new energy states of bilayer system are depicted graphically in Fig. 3. We divide them on spin-up (left) and spin-down (right) subsets for clarity. The single and doubled bumps in the figure represent the new CB and VB states. The size of the bump describes the probability to observe the new composite quasiparticle in the bottom (green part) or the top (red part) layers. Note that the valence band states can be found in both layers. That makes these states optically active in both polarizations. Namely, the transitions from any valence band state into $|\Psi_c^{(1)}\rangle$ and $|\Psi_c^{(2)}\rangle$ states are possible in σ^+ and σ^- circularly polarised light, respectively. In consequence, the system demonstrates four types of optically active exciton resonances — two intralayer and two inter-

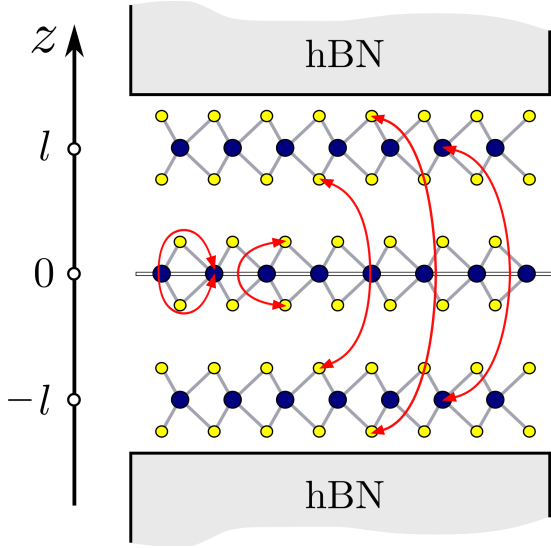


FIG. 4. The trilayer crystal embedded in between two thick hBN flakes, side view. The mirror symmetry plane $z = 0$ is represented by thin rectangular. The ends of red curly arrows couple the atoms, which coordinates transform to each other after mirror symmetry transformation operation.

layer ones. The half of all transitions — $T_A(T_B)$ between spin-up (spin-down) bands are presented in Fig. 3.

There are two intralayer exciton transitions in bilayer

$$T_A : \begin{cases} |\Phi_{v\uparrow}^+\rangle \rightarrow |\Psi_c^{(1)}\rangle \otimes |\uparrow\rangle, \\ |\Phi_{v\downarrow}^+\rangle \rightarrow |\Psi_c^{(2)}\rangle \otimes |\downarrow\rangle; \end{cases} \quad (4)$$

$$T_B : \begin{cases} |\Phi_{v\uparrow}^-\rangle \rightarrow |\Psi_c^{(2)}\rangle \otimes |\uparrow\rangle, \\ |\Phi_{v\downarrow}^-\rangle \rightarrow |\Psi_c^{(1)}\rangle \otimes |\downarrow\rangle. \end{cases} \quad (5)$$

All of them have the same intensity $I = I_0 \cos^2 \theta$, where I_0 is the intensity of exciton line in monolayer.

There are two interlayer exciton transitions in bilayer

$$T'_A : \begin{cases} |\Phi_{v\uparrow}^+\rangle \rightarrow |\Psi_c^{(2)}\rangle \otimes |\uparrow\rangle, \\ |\Phi_{v\downarrow}^+\rangle \rightarrow |\Psi_c^{(1)}\rangle \otimes |\downarrow\rangle; \end{cases} \quad (6)$$

$$T'_B : \begin{cases} |\Phi_{v\uparrow}^-\rangle \rightarrow |\Psi_c^{(1)}\rangle \otimes |\uparrow\rangle, \\ |\Phi_{v\downarrow}^-\rangle \rightarrow |\Psi_c^{(2)}\rangle \otimes |\downarrow\rangle. \end{cases} \quad (7)$$

They have the intensities $I' = I_0 \sin^2 \theta$. Finally, since the intra- and inter-layer exciton transitions are active in opposite circular polarization at a given K point, they should have the opposite signs of g -factors (see Appendix B).

For a *trilayer* case, a crystal can be presented as three monolayers each separated by distance l , with the middle layer is 180° rotated around the external ones (see Fig. 4). Similarly to the bilayer case, we focus on properties of quasiparticles at the K^+ point. The basis states

of a trilayer are $\{|\Psi_n^{(1)}\rangle \otimes |s\rangle, |\Psi_n^{(2)}\rangle \otimes |s\rangle, |\Psi_n^{(3)}\rangle \otimes |s\rangle\}$. They belong to $z = -l, z = 0$ and $z = l$ layers, respectively. In this case, the crystal has mirror symmetry σ_h , with the mirror plane $z = 0$. It determines the symmetry relations $|\Psi_n^{(3)}\rangle = \sigma_h |\Psi_n^{(1)}\rangle, |\Psi_n^{(2)}\rangle = \sigma_h |\Psi_n^{(2)}\rangle$. The properties of $|\Psi_n^{(1)}\rangle$ and $|\Psi_n^{(2)}\rangle$ states are the same as in bilayer discussed in the main text. The properties of $|\Psi_n^{(3)}\rangle$ states coincide with $|\Psi_n^{(1)}\rangle$ according to the crystal symmetry. Hence, in K^+ point, the 1-st and 3-d layers absorb only σ^+ polarised light, while the 2-nd one is active in σ_- polarization. Note that the trilayer encapsulated in between to equal hBN flakes conserves the mirror symmetry.

We derive the effective $\mathbf{k} \cdot \mathbf{p}$ Hamiltonian for considering system within several approximations: *i*) the interlayer spin-orbit coupling between CB and VB states with opposite spins from different layers is neglected, like in bilayer; *ii*) the intralayer crystal field corrections are equal for each layer, *i.e.* the bands of each layer are characterised by the same band-gap E_g and spin-splitting Δ_v, Δ_c parameters, the magnitudes of which, however, can deviate from their bilayer analogs; *iii*) we neglect the coupling between the states of the 1-st and 3-d layers. In this approach, like in bilayer case, the spin-up and spin-down states of trilayer are decoupled. The Hamiltonian for VB states, written in the basis $\{|\Psi_v^{(1)}\rangle \otimes |s\rangle, |\Psi_v^{(2)}\rangle \otimes |s\rangle, |\Psi_v^{(3)}\rangle \otimes |s\rangle\}$, is

$$H_{vs}^{(3)} = \begin{bmatrix} \sigma_s \frac{\Delta_v}{2} & t & 0 \\ t & -\sigma_s \frac{\Delta_v}{2} & t \\ 0 & t & \sigma_s \frac{\Delta_v}{2} \end{bmatrix}. \quad (8)$$

The Hamiltonian for conduction bands, written in the basis $\{|\Psi_c^{(1)}\rangle \otimes |s\rangle, |\Psi_c^{(2)}\rangle \otimes |s\rangle, |\Psi_c^{(3)}\rangle \otimes |s\rangle\}$, reads

$$H_{cs}^{(3)} = \begin{bmatrix} E_g + \sigma_s \frac{\Delta_c}{2} & uk_+ & 0 \\ uk_- & E_g - \sigma_s \frac{\Delta_c}{2} & uk_- \\ 0 & uk_+ & E_g + \sigma_s \frac{\Delta_c}{2} \end{bmatrix}. \quad (9)$$

The system possesses a mirror symmetry. Hence, it is convenient to introduce the new basis states which are even $|\Upsilon_n^{(1)}\rangle = \frac{1}{\sqrt{2}}[|\Psi_n^{(1)}\rangle + |\Psi_n^{(3)}\rangle], |\Upsilon_n^{(2)}\rangle = |\Psi_n^{(2)}\rangle$ and odd $|\Upsilon_n^{(3)}\rangle = \frac{1}{\sqrt{2}}[|\Psi_n^{(1)}\rangle - |\Psi_n^{(3)}\rangle]$ under σ_h transformation. The trilayer Hamiltonians have a block-diagonal form in the basis $\{|\Upsilon_n^{(1)}\rangle \otimes |s\rangle, |\Upsilon_n^{(2)}\rangle \otimes |s\rangle, |\Upsilon_n^{(3)}\rangle \otimes |s\rangle\}$

$$\mathcal{H}_{vs}^{(3)} = \begin{bmatrix} \sigma_s \frac{\Delta_v}{2} & \sqrt{2}t & 0 \\ \sqrt{2}t & -\sigma_s \frac{\Delta_v}{2} & 0 \\ 0 & 0 & \sigma_s \frac{\Delta_v}{2} \end{bmatrix}, \quad (10)$$

$$\mathcal{H}_{cs}^{(3)} = \begin{bmatrix} E_g + \sigma_s \frac{\Delta_c}{2} & \sqrt{2}uk_+ & 0 \\ \sqrt{2}uk_- & E_g - \sigma_s \frac{\Delta_c}{2} & 0 \\ 0 & 0 & E_g + \sigma_s \frac{\Delta_c}{2} \end{bmatrix}. \quad (11)$$

The 2×2 blocks have the structure of bilayer Hamiltonians. Therefore, all the properties of the trilayer even

states can be obtained from bilayer result by replacing $t \rightarrow \sqrt{2}t, u \rightarrow \sqrt{2}u$. Consequently, there are doubly degenerate valence and conduction bands, which define the intensive T_A and T_B and weak T'_A and T'_B groups excitonic transitions, which are active in opposite polarizations of light (see Fig. 5(a)). The 1×1 block has the structure of monolayer Hamiltonian. Hence, there are only T_A^o and T_B^o transitions between odd states of trilayer. They are active in the same polarization as T_A and T_B transitions of monolayer (see Fig. 5(b)). Summarising, the trilayer possesses two types of "even" intralayer excitons — T_A and T_B , two types of "odd" intralayer ones — T_A^o and T_B^o . All of them are active in σ^+ polarization at the K^+ point and have the g -factors of the same sign. The interlayer "even" excitons — T'_A and T'_B , conversely are active in σ^- polarization at the K^+ point and have an opposite sign to intralayer excitons g -factors. The detailed description of trilayer's g -factors is presented in Appendix C.

Note that the current theoretical description predicts the number of exciton resonances and their polarization properties. However, the relative position of T_A and T_A^o exciton remains an open question. Indeed, both lines are active in the same polarization and have similar g -factors, that makes impossible to identify each of them from the experiment. The analysis of the interference effects together with the consideration of the Coulomb interaction between new quasiparticles answers this question, which is, however, beyond the scope of the current paper. In our case, we took the position of exciton resonances following the position of the valence and conduction bands, derived in single-particle $\mathbf{k} \cdot \mathbf{p}$ approximation, for definiteness.

Our single-particle considerations are summarized in Fig. 6. This picture exhibits the position and number of optically active transitions in mono-, bi- and trilayer S-TMD crystals.

III. ABSORPTION RESONANCES IN MoS_2 MULTILAYERS

In the experiments, we have investigated a set of van der Waals heterostructures with optically active parts consisting of MoS_2 mono- (1ML), bi- (2ML) and trilayer (3ML). The structures were prepared on ultraflat unoxidized silicon substrates by combination of exfoliation and dry transfer techniques [48]. In order to achieve the highest possible quality of our samples, as well as to preserve the characteristic inverse and mirror symmetries of, respectively, 2H-stacked bi- and trilayer, the microcleaved MoS_2 flakes were sandwiched between two hBN flakes exfoliated from high-quality bulk crystals grown under high-pressure conditions [49]. Further information on the preparation of samples and their characterization is provided in Appendix A.

Experiments consisted of measurements of the re-

flectance contrast spectra, which are defined as

$$RC(E) = \frac{R(E) - R_0(E)}{R(E) + R_0(E)} \times 100\%, \quad (12)$$

where $R(E)$ is the reflectance spectrum when the light is focused on the MoS_2 flake and $R_0(E)$ is the reflectance from the region outside the flake. Two different micro-optical setups have been used for measurements: one setup for measurements in the absence of magnetic fields and the second one for measurements in magnetic fields supported by either a 14 T superconducting magnet or a 29 T resistive magnet. A spatial resolution of about $1 \mu\text{m}$ (light spot diameter) is characteristic of our free-beam-optics setup used for experiments at zero magnetic field. Instead, the fiber-optics-based arrangement applied for experiments in magnetic fields provides a poorer spatial resolution, of about $10 \mu\text{m}$. A spectral resolution of 0.32 nm has been assured for both setups. A combination of a quarter wave plate and a polarizer are used to analyse the circular polarization of signals. The measurements are performed with a fixed circular polarization, whereas reversing the direction of magnetic field yields the information corresponding to the other polarization component due to time-reversal symmetry. More on experimental details can be found in Appendix A.

The collection of low temperature ($\sim 5 \text{ K}$) RC spectra using our $B = 0$ setup, measured in the spectral range of the optical gap (onset of strong absorption) of the MoS_2 layers is presented in Fig. 7. The observed, more or less pronounced resonances, show the dispersive spectral shape, correspond to typically, strongly bound direct bandgap excitons in S-TMD layers. Although our theoretical considerations neglect the effects of Coulomb binding and account only for interband transitions, a distinct resemblance between the measured spectral evolution (Fig. 7) and that theoretically concluded in Fig. 6 can be recognized.

In the following we assume that each interband transition T_X is associated with the corresponding excitonic resonance X and we proceed with the assignment of the resonances observed in the experiment. We suppose that the resonating excitons are shifted in energy, by their binding energies, with respect to the associated interband transitions: $E(X) = E(T_X) - E_b(X)$. Binding energies might be, however, different for different excitons and this fact must be taken into account when comparing the energy position of X -resonances and T_X -transitions. Important for the assignment of the observed resonances are the results of the polarization resolved measurements carried out in magnetic fields (see Figs. 8 and 9). As discussed above, we expect that our multilayers host two different types of intra- and interlayer excitons, each of them being distinguishable by their different polarization properties (g -factors of opposite sign and various magnitudes). At this point we must admit that all subtle spectral features which are well visible in the RC spectra measured at $B = 0$ with high spatial resolution are somewhat less pronounced in the magneto-optical measure-

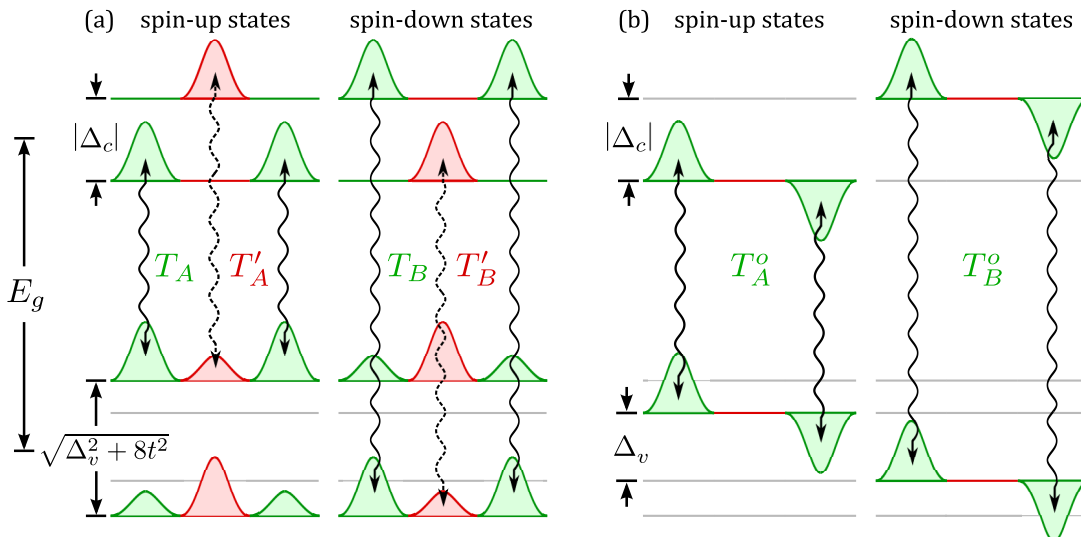


FIG. 5. Sketch of bands positions and optical transitions between (a) even and (b) odd states at the K^+ of the BZ in a bilayer of MoS_2 . Green and red bump structures represent conduction and valence band states associated with transitions active correspondingly in the σ^+ and σ^- polarizations. Solid (dashed) wavy arrows denote optical transitions due to the intralayer (interlayer) A and B excitons. $|\Delta_c|$ and $\sqrt{\Delta_v^2 + 8t^2}$ (Δ_v) denote the splitting in the CB and even (odd) states of VB, respectively. E_g is the single particle band gap.

ments which imply worse spatial resolution. Certain degree of sample inhomogeneity is an obvious cause of this drawback. In consequence, in the case of weak and/or broad resonances the information about their g -factors is not easily extractable from the raw magneto-RC data. This information becomes more apparent if we inspect the RC-polarization spectra. These spectra have been constructed as a difference between the RC-spectra measured at the same strength but for two opposite direction of the magnetic field (that mimic, due to the time reversal symmetry, the spectra corresponding to σ^+ and σ^- circular polarization of the reflected light [39, 50]). As can be deduced from the data shown in Figs. 8 and 9, the apparent dips in our RC polarization spectra correspond to excitonic resonances with negative g -factors whereas the characteristic upswings mark the resonances with positive g -factors.

Very first classification of the observed resonance takes into account a relatively large spin-orbit splitting in the MoS_2 valence band, rising two groups of excitons associated with well-separated upper (A -excitons) and lower (B -excitons) valence band subbands. The 1ML spectrum shown in Fig. 7, resembles that previously reported for a high quality 1ML MoS_2 encapsulated in hBN [44, 51]. It depicts three resonances: one well-separated resonance due A -exciton (ground state), X_A , and two other superimposed resonances, due to B -exciton (X_B) and the first excited ($2s$) state of A -exciton (X_A^{2s}). X_A and X_B resonances are associated with T_A and T_B transitions sketched in Fig. 1; the excited excitonic states are beyond the frame of our single particle theoretical approach. As expected, the X_A , X_B and X_A^{2s} excitonic resonances display similar polarization properties in the

magneto-optical experiments (see Fig. 8). We estimate $g_{X_A} \approx -4$ in agreement with previous reports [52–54]; the accurate estimation of the amplitudes of g_{X_B} and $g_{X_A^{2s}}$ is more cumbersome though both these values are also negative.

The RC spectrum of the 2ML (Fig. 7) shows 4 resonances [38] which, in reference to our theoretical expectations (see Figs. 3 and 6), are assigned to the pair of intra- (X_A) and interlayer (X'_A) A -excitons, and to the analogous pair of intra- (X_B) and interlayer (X'_B) B -excitons. We use the signs and magnitude of the exciton g -factors as fingerprints the intra- and interlayer nature of the X_A - and X'_A -excitons respectively [39]. Namely, we conclude that $g_{X_A} \approx -4$, while $g_{X'_A} \approx 8$. Again, the exact values for the g -factor amplitudes of B -excitons are hard to be precisely estimated. Nonetheless it is rather clear that g_{X_B} is negative whereas $g_{X'_B}$ is positive. Whereas our theoretical model meets the experimental data at the qualitative level, the energy ladder of the observed resonances requests further comments. Characteristic for the theoretical modelling is the fact that the energy distance, $\Delta(T'_A, T_A)$, between the T'_A and T_A transitions is the same as the energy separation, $\Delta(T_B, T'_B)$ between the T_B and T'_B transitions, both differences being determined by the amplitude Δ_c of the spin orbit splitting in the conduction band of the 2ML: $\Delta(T'_A, T_A) = \Delta(T_B, T'_B) = |\Delta_c|$. This property is not seen in the experiment: we estimate that $\Delta(X'_A, X_A) \simeq 70$ meV, whereas $\Delta(X_B, X'_B) \simeq 30$ meV. The inconsistency between theory and experiment is likely due to different binding energies of excitons associated with different interband transitions: $E(X) = E(T_X) - E_b(X)$. In the first approximation we assume that binding en-

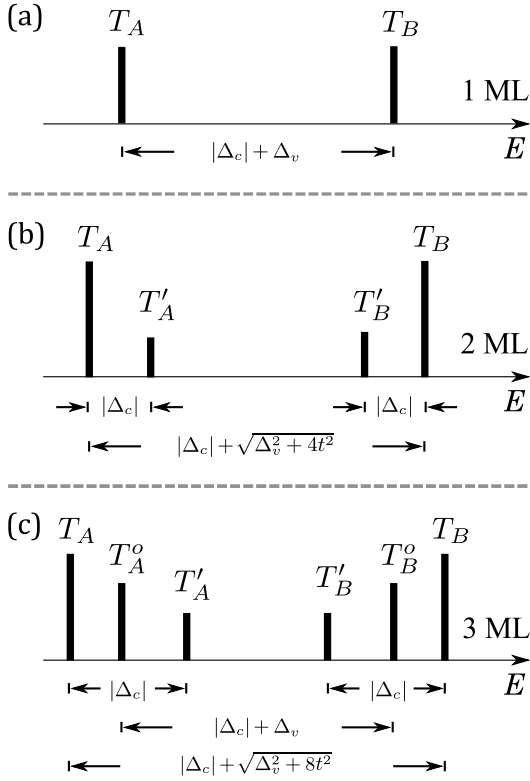


FIG. 6. Sketch of optical transitions in (a) mono-, (b) bi- and (c) trilayer S-TMD crystals. The position and size of black thick segments represent the energies and intensities of the corresponding transitions. The values of parameters Δ_c and Δ_v for bilayer and trilayer can deviate from their monolayer analogs.

ergies of our inter- and intralayer excitons are indeed different but that the excitons within each pair of indirect and direct resonances are the same: $E_b(X_A) = E_b(X_B) \neq E_b(X'_A) = E_b(X'_B) = E_b(\text{inter})$. Then, comparing the theoretical prediction with the experimental data one obtains that $|\Delta_c| = \Delta(T'_A, T_A) = \Delta(T_B, T'_B) = [\Delta(X'_A, X_A) + \Delta(X_B, X'_B)]/2 \simeq 50$ meV and that $E_b(\text{intra}) = E_b(\text{inter}) + 20$ meV. Larger binding energies of intralayer excitons with respect to those of interlayer excitons are logically expected since Coulomb attraction should be indeed stronger/weaker when the electron and hole charges are localized in the same or in the neighboring layers, as for the case of intra- or interlayer excitons, respectively. At first sight, the estimated amplitude of the spin orbit splitting in the conduction band of the MoS₂ bilayer appears to be surprisingly large. In the case of 1L MoS₂, the commonly accepted results of the DFT calculations predict Δ_c in the range of few meV, though recent experimental works point out towards much higher values of about 15 meV [55]. According to our theoretical approach, the spin orbit interaction is sensitive to interlayer coupling and it is also affected by the interaction with the surrounding material (hBN). Thus the amplitudes of the Δ_c as well as Δ_v parameters

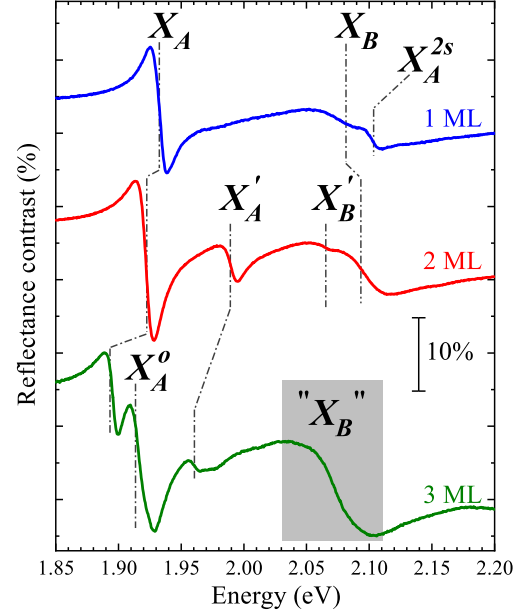


FIG. 7. Reflectance contrast spectra of MoS₂ layers encapsulated in hBN measured at $T=5$ K. The spectra are vertically shifted for clarity.

are expected to evolve with the numbers of the stacked MoS₂ layers. Keeping our assumption about equal binding energies for X_A and X_B excitons we note that the expected energy separation between these excitonic resonances is given by $|\Delta_c| + \sqrt{\Delta_v^2 + 4t^2}$ (see Figs. 3 and 6), to be compared to the value of 170 meV estimated from the experiment. With the theoretically estimated value of $t \simeq 40$ meV [30] and the derived above $|\Delta_c| \simeq 50$ meV we find $\Delta_v \simeq 90$ meV. Visibly, however, the “effective” spin orbit splitting in the valence band of the MoS₂ bilayer is larger, as given by $\sqrt{\Delta_v^2 + 4t^2} \simeq 120$ meV (see Fig. 3).

Focusing now on the trilayer spectra (see bottom panel of Fig. 7) we observe a characteristic triplet of A -exciton resonances, which is in accordance with our theoretical expectations (see Fig. 6c). As expected, two strong X_A and X_A^o resonances are characterised by negative g -factors whereas the g -factor of the interlayer X'_A exciton is pretty much positive. The theoretically anticipated triplet structure of the “ X_B^o ”-exciton is not resolved in the experiment but likely hidden within the observed broad spectrum of the B -exciton. Even with unresolved fine structure of the B -exciton for our trilayer MoS₂, a rough estimation of Δ_c and Δ_v parameters can be done. Expecting that the energy separation between X'_A and X_A is $\Delta(X'_A, X_A) = |\Delta_c| + E_b(X_A) - E_b(X'_A)$ and reading $\Delta(X'_A, X_A) \simeq 70$ meV from the experiment we conclude that $|\Delta_c| \simeq 50$ meV if the difference between binding energies of the intralayer X_A and interlayer X'_A excitons is $E_b(X_A) - E_b(X'_A) \simeq 20$ meV, *i.e.* the same as we found for intra- and interlayer excitons in 2ML MoS₂. On the other hand, supposing that

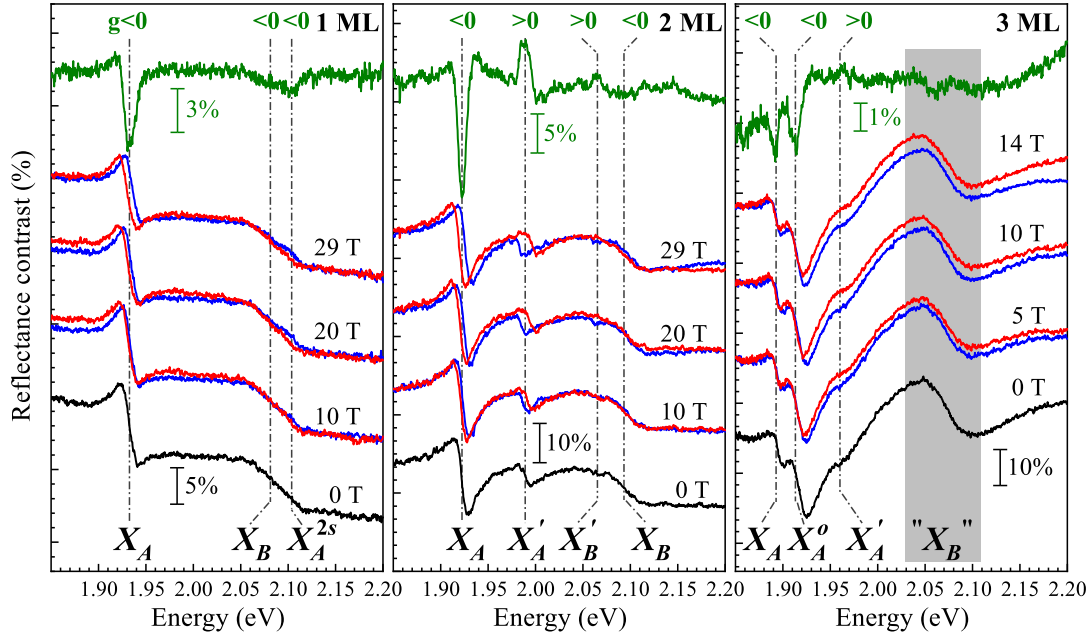


FIG. 8. Helicity-resolved reflectance contrast spectra of MoS₂ layers encapsulated in hBN for selected values of magnetic field measured at $T=4.2$ K. The red and blue curves correspond to σ^+ polarization of reflected light in B and $-B$ configurations of magnetic field (applied perpendicularly to the layers plane), respectively. The spectra are vertically shifted for clarity.

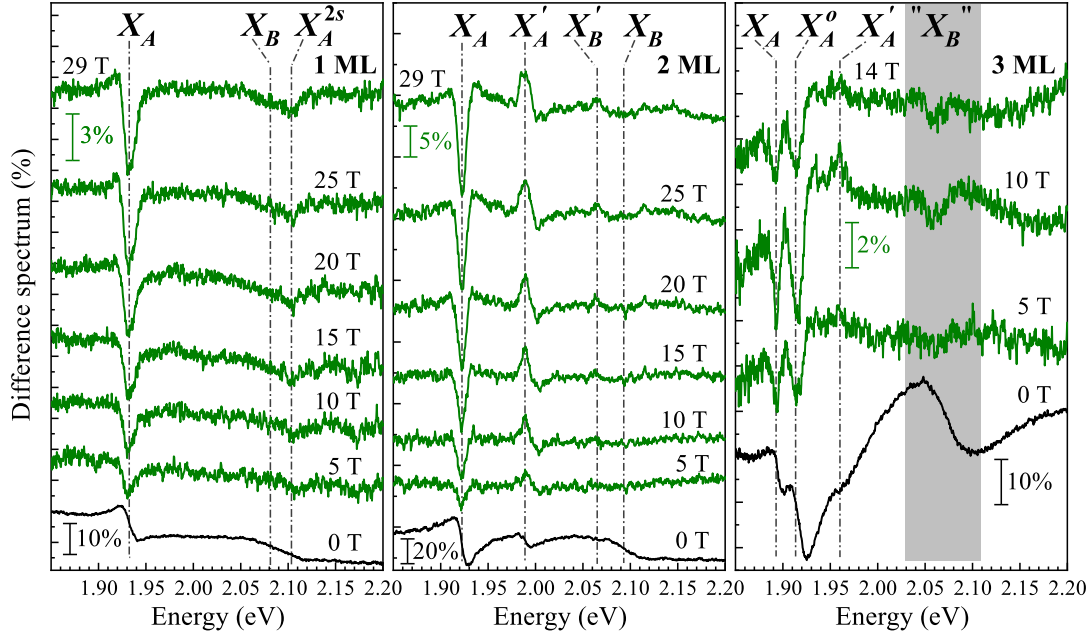


FIG. 9. Zero-field RC spectra (black) with difference spectra $[RC(\sigma^+, B) - RC(\sigma^+, -B)]$ at selected values of B field for 1ML (left panel), 2ML (middle panel) and 3ML (right panel) MoS₂ encapsulated in hBN. A deep in the difference spectra indicate a negative g -factor, while a peak indicates a positive g -factor.

binding energies of two X_A and X_A^o intralayer excitons are the same we expect that they are separated in energy by $\Delta(X_A^o, X_A) = (\sqrt{\Delta_v^2 + 8t^2} - \Delta_v)/2$ and extract $\Delta_v \simeq 140$ meV when reading $\Delta(X_A^o, X_A) \simeq 20$ meV from the experiments and assuming again that $t \simeq 40$ meV.

With the above estimation, the band-edge structure of the 3L MoS₂ at the K^\pm points of the Brillouin zone is concluded to consist of two conduction band subbands split by 50 meV and 4 valence band subbands with outer two subbands split by 180 meV and the inner two sub-

bands split by 140 meV.

IV. CONCLUSION

We have performed magneto-optical μ -reflectance measurements along with $\mathbf{k} \cdot \mathbf{p}$ theory based modelling on few-layer MoS₂ encapsulated in hBN structures, revealing the intralayer and interlayer nature of the newly discovered transitions. Such resonances form due to hybridisation of valence and conduction bands states when one adds new layers to the system.

The experiment *i*) manifests the new exciton resonances and their number in bi- and trilayers; *ii*) demonstrates that g -factors of intralayer and interlayer transitions have opposite signs; *iii*) the g -factor values of the latter ones are much larger (by magnitude) than of the former ones.

The symmetry based $\mathbf{k} \cdot \mathbf{p}$ description of the bi- and trilayers gives the natural explanation of the aforementioned experimental observations. Moreover, from the general symmetry point of view the theoretical model also predicts *i*) the renormalization of the band gap E_g and spin splittings Δ_c, Δ_v ; *ii*) the deviation of the bi- and trilayer exciton g -factors from their monolayer analogs. These two phenomena appear as a result of the coupling between different layer of the system and effects of dielectric screening induced by hBN.

Finally, we point out some unique properties of the exciton states of the trilayer. First, we mention the existence of two groups of exciton resonances — “even” and “odd”, which do not interact with each other because they belong to different irreps of the in-plane mirror symmetry of the system. However, electric field, applied perpendicularly to the crystal’s plane, violates this symmetry and causes the controllable coupling of these states. Such feature can be used in future exciton based applications. We also note that the electrical positive and negative charges of interlayer excitons are separated between different layers. Such a property can be interesting in photovoltaic applications of S-TMD systems.

ACKNOWLEDGEMENTS

The work has been supported by the ATOMOPTO project (TEAM programme of the Foundation for Polish Science co-financed by the EU within the ERDFund), the EC Graphene Flagship project (no. 604391), the National Science Centre (grants no. DEC-2013/10/M/ST3/00791, UMO-2017/24/C/ST3/00119), the Nanofab facility of the Institut Néel, CNRS UGA and LNCMI-CNRS, a member of the European Magnetic Field Laboratory (EMFL).

Appendix A: Samples and experimental setups

In order to provide even and charged-defect-free support to van der Waals heterostructures studied in this work we assembled them on ultraflat unoxidized silicon (Si) substrates from Ted Pella Inc., whose surface roughness amounts to about one-tenth of that of standard Si/SiO₂ wafers. Each heterostructure consisted of three flakes obtained by means of mechanical exfoliation and successively stacked one on top of another using dry transfer techniques: a 60-70 nm thick bottom hBN flake, a central MoS₂ flake of 1ML, 2ML or 3ML thickness, and a 10-15 nm thick top hBN flake.

The optimum thicknesses of hBN flakes were estimated on the basis of transfer-matrix simulations of reflectance contrast spectra of complete heterostructures, aiming at maximizing the visibility of absorption resonances in MoS₂ flakes while keeping the thickness of bottom hBN flakes below 100 nm (a value up to which our exfoliation method yields a rich harvest of flat, defect-free flakes with large-area terraces of constant thickness).

Using high-purity ELP BT-150E-CM tape from Nitto Denko, bottom hBN flakes were exfoliated from high-quality bulk crystals grown under high-pressure conditions [49] and then transferred in a non-deterministic way onto clean and freshly annealed at 200°C Si substrates. The MoS₂ flakes were obtained by means of two-stage, tape- and polydimethylsiloxane (PDMS)-based exfoliation of a bulk crystal purchased from HQ Graphene and then stacked on the bottom hBN flakes using an all-dry deterministic stamping technique [48]. The same procedure was applied also to the top hBN flakes. While performing deterministic transfers, special attention was paid to mutual angular alignment of the flakes and to immediate 10-minute-long after-transfer annealing of the samples at 180°C on a hot plate kept in clean ambient atmosphere.

Optical microscope images of investigated heterostructures which were fabricated in this way are shown in Fig. 10 (a)-(c). The spots of brown-to-blue colour visible in all images are up to 60-nm-high bubbles of air and/or water vapour (possibly with some amount of hydrocarbons) trapped between either the MoS₂ and the top hBN flake or the two hBN flakes. Their appearance directly results from the corrugation of thin, soft and flexible top hBN flakes supported by a PDMS stamp. Importantly, the areas between the bubbles, whose size reaches up to 5 by 10 micrometers, exhibit very flat and high-quality interfaces between the constituent flakes, as revealed with optical measurements and atomic force microscopy (AFM) characterization.

An example of tapping-mode AFM imaging performed on finished heterostructures with the use of Digital Instruments Dimension 3100 microscope is shown in Fig. 10 (d)-(f). The false colour AFM images correspond to respective locations marked in panels (a)-(c) with orange circles. The grey arrows represent the line profiles drawn in Fig. 10 (g) and labelled with the same numbers as in

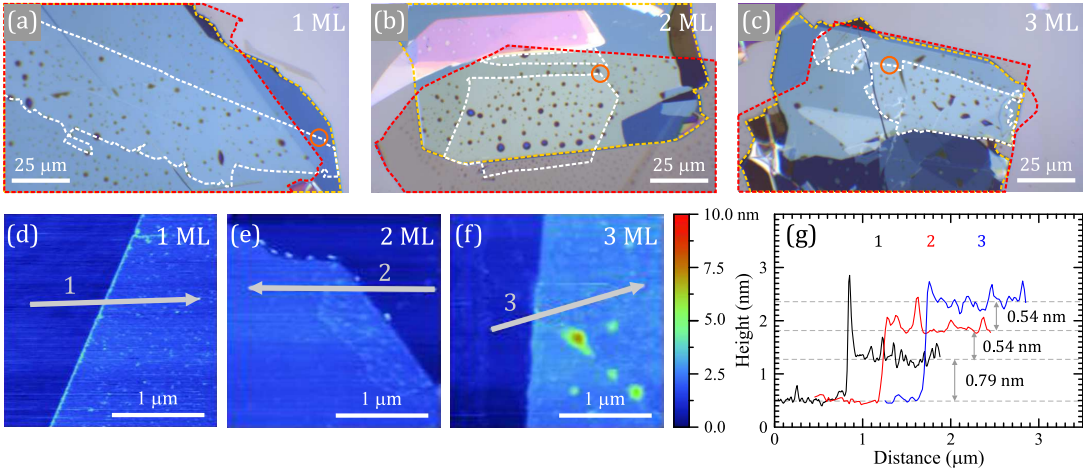


FIG. 10. Upper row: optical microscope images of hBN/MoS₂/hBN heterostructures comprising (a) mono-, (b) bi- and (c) trilayer MoS₂ flakes (outlined in white) sandwiched between two hBN flakes – a 60-70 nm thick flake from the bottom (outlined in yellow) and 10-15 nm thick flake from the top (outlined in red). The spots of brown-to-blue colour visible in all images are bubbles of air and/or water vapour trapped between either the MoS₂ and the top hBN flake or the two hBN flakes. Lower row: (d)-(f) false colour atomic force microscope images taken at respective locations marked in (a)-(c) with orange circles. The grey arrows represent the line profiles drawn in panel (g) and labelled with the same numbers as in images (d)-(f).

images (d)-(f). As can be seen, the profiles unambiguously confirm the mono-, bi-, and trilayer thickness of MoS₂ flakes incorporated into the heterostructures shown in the upper row of Fig. 10.

Compared to based on neutron scattering measurements estimation equal to 0.615 nm [56], the value of 0.79 nm we got for the monolayer most probably indicates that the equilibrium distance between the hBN and MoS₂ layers differs from that between two neighboring MoS₂ layers in a bulk crystal. A smaller single-layer step height obtained for the second and third layer in the bi- and trilayer MoS₂ flakes may on the other hand imply the existence of small uniaxial compressive strain along the *c*-axis in hBN/MoS₂/hBN heterostructures.

Measurements at zero magnetic field were carried out with the aid of a continuous flow cryostat mounted on *x* – *y* motorized positioners. The samples were placed on a cold finger of the cryostat. The temperature of the samples was kept at *T* = 5 K. The excitation light was focused by means of a 50x long-working distance objective with a 0.5 numerical aperture producing a spot of about 1 μm. The signal was collected via the same microscope objective, sent through a 0.5 m monochromator, and then detected by a CCD camera.

Magneto-optical experiments were performed in the Faraday configuration using an optical-fiber-based insert placed in a resistive or a superconducting magnet producing magnetic fields up to 29 T or 14 T, respectively. The sample was mounted on top of an *x* – *y* – *z* piezo-stage kept in gaseous helium at *T*=4.2 K. The μ-RC experiments were performed with the use of 100 W tungsten halogen lamp. The excitation light was coupled to an optical fiber with a core of 50 μm diameter and focused on the sample by an aspheric lens (spot diameter around 10

μm). The signal was collected by the same lens, injected into a second optical fiber of the same diameter, and analyzed by a 0.5 m long monochromator equipped with a CCD camera. A combination of a quarter wave plate and a polarizer are used to analyse the circular polarization of signals.

Appendix B: Bilayer in magnetic field

The magnetic field correction to the valence band Hamiltonian at the K⁺ point written in the basis $\{|\Psi_v^{(1)}\rangle \otimes |s\rangle, |\Psi_v^{(2)}\rangle \otimes |s\rangle\}$ is $\delta H_{vs}^{(2)} = (G_v^{(2)} + \sigma_s \mathbb{1})\mu_B B$. Here μ_B is the Bohr magneton, *B* is the magnetic field, applied perpendicularly to the bilayer plane, $\mathbb{1}$ is the unit matrix and

$$G_v^{(2)} = \begin{bmatrix} g_v - \delta g_v & 0 \\ 0 & -g_v + \delta g_v \end{bmatrix}. \quad (\text{B1})$$

The correction to the conduction band Hamiltonian written in the basis $\{|\Psi_c^{(1)}\rangle \otimes |s\rangle, |\Psi_c^{(2)}\rangle \otimes |s\rangle\}$ has the same form $\delta H_c^{(2)} = (G_c^{(2)} + \sigma_s \mathbb{1})\mu_B B$, where

$$G_c^{(2)} = \begin{bmatrix} g_c - \delta g_c & 0 \\ 0 & -g_c + \delta g_c \end{bmatrix} \mu_B B. \quad (\text{B2})$$

The expressions for g_v , g_c , δg_v , δg_c are derived in [37]. The corrections to the Hamiltonians provide the energy shifts of excitons in magnetic field. The intralayer X_A and X_B excitons, constructed from the quasiparticles at the K⁺ point of bilayer, are active in σ^\pm polarizations. The corresponding energy shifts are linear in magnetic field $\delta E_{A,B}^{\sigma^\pm} = \pm g_{A,B}^{(2)} \mu_B B$. The *g*-coefficients of such

exciton transitions are

$$g_A^{(2)} = -g_u + (g_c - \delta g_c) - (g_v - \delta g_v) \frac{\Delta_v}{\sqrt{\Delta_v^2 + 4t^2}}, \quad (\text{B3})$$

$$g_B^{(2)} = g_u + (g_c - \delta g_c) - (g_v - \delta g_v) \frac{\Delta_v}{\sqrt{\Delta_v^2 + 4t^2}}. \quad (\text{B4})$$

We introduced $g_u = 2m_0u^2/\hbar^2\Delta_c$ parameter, which originates from k -dependent admixture of conduction bands. The mixing is negligibly small in the absence of magnetic field, but gives finite correction if $B \neq 0$. The interlayer excitons X'_A and X'_B at the bilayer K^+ point are also active in σ^\pm polarizations with the magnetic shifts $\delta E_{A',B'}^{\sigma^\pm} = \pm g_{A',B'}^{(2)}\mu_B B$ respectively. The corresponding g -coefficients are

$$g_{A'}^{(2)} = g_u + (g_c - \delta g_c) + (g_v - \delta g_v) \frac{\Delta_v}{\sqrt{\Delta_v^2 + 4t^2}}, \quad (\text{B5})$$

$$g_{B'}^{(2)} = -g_u + (g_c - \delta g_c) + (g_v - \delta g_v) \frac{\Delta_v}{\sqrt{\Delta_v^2 + 4t^2}}. \quad (\text{B6})$$

Note that there are the following relations between g -coefficients of interlayer and intralayer exciton transitions

$$g_A^{(2)} + g_{A'}^{(2)} = g_B^{(2)} + g_{B'}^{(2)} = 2(g_c - \delta g_c), \quad (\text{B7})$$

$$g_{A'}^{(2)} - g_B^{(2)} = g_{B'}^{(2)} - g_A^{(2)} = (g_v - \delta g_v) \frac{2\Delta_v}{\sqrt{\Delta_v^2 + 4t^2}}, \quad (\text{B8})$$

$$g_B^{(2)} - g_A^{(2)} = g_{A'}^{(2)} - g_{B'}^{(2)} = 2g_u. \quad (\text{B9})$$

One can mention that the corresponding transitions at the K^- point in σ^\pm polarizations are characterized by the same values $\pm g_{A,B}^{(2)}$ and $\pm g_{A',B'}^{(2)}$ as in K^+ point. This is the consequences of time reversal and inversion symmetries of the crystal. As a result, we can restore the absorption spectra of the bilayer in σ^- and σ^+ polarizations using our methodology of the experiment — by measuring the reflected light in fixed σ^+ polarization and changing the orientation of magnetic field from B to $-B$. The change of the direction of the magnetic field to $-B$ in experiment mimics the transitions in σ^- polarization of the reflected light.

We use the formula $g = [E^{\sigma^+}(B) - E^{\sigma^+}(-B)]/\mu_B B = [\delta E^{\sigma^+}(B) - \delta E^{\sigma^+}(-B)]/\mu_B B$ for exciton's g -factor. As a result the intralayer and interlayer A, B excitons have $2g_{A,B}^{(2)}$ and $2g_{A',B'}^{(2)}$ g -factors, respectively.

The possible signs of intra- and interlayer exciton g -factors can be obtain from the expressions (B3), (B4), (B5) and (B6). Indeed, in the experiment we have $2g_{A,B}^{(2)} \approx -4$. It means that corrections g_u , δg_c and δg_v are not significantly large, and therefore very roughly $2g_{A,B}^{(2)} \approx 2(g_c - g_v)$ is nothing but the g -factors of monolayer A and B excitons, for which we know that $g_v > g_c > 0$. Substituting the positive g_c and g_v into Eqs. (B5) and (B6) one can see that $2g_{A',B'}^{(2)} > 0$, which is confirmed from the experiment.

Appendix C: Trilayer in magnetic field

The magnetic field correction to the valence and conduction band Hamiltonians written in the basis $\{|\Psi_n^{(1)}\rangle \otimes |s\rangle, |\Psi_n^{(2)}\rangle \otimes |s\rangle, |\Psi_n^{(3)}\rangle \otimes |s\rangle\}$, is $\delta H_{ns}^{(3)} = (G_n^{(3)} + \sigma_s \mathbb{1})\mu_B B$ where

$$G_n^{(3)} = \begin{bmatrix} g_n - \delta g_n & 0 & \bar{g}_n \\ 0 & -g_n + 2\delta g_n & 0 \\ \bar{g}_n & 0 & g_n - \delta g_n \end{bmatrix}, \quad (\text{C1})$$

Here $n = v, c$ and \bar{g}_c and \bar{g}_v are the additional parameters which describe the magnetic dependent coupling between layers of the system [37]. In new basis, defined in the main part of the text, the full Hamiltonians $H_{ns}^{(3)} + \delta H_{ns}^{(3)}$ are reduced to a block-diagonal form. Namely, the $G_n^{(3)}$ matrix transforms to

$$G_n^{(3)} = \begin{bmatrix} g_n - \delta g_n + \bar{g}_n & 0 & 0 \\ 0 & -g_n + 2\delta g_n & 0 \\ 0 & 0 & g_n - \delta g_n - \bar{g}_n \end{bmatrix}. \quad (\text{C2})$$

The 1×1 block corresponds to odd states $|\Upsilon_{ns}^{(3)}\rangle \otimes |s\rangle$ with total energies

$$E_{ns}^o(B) = E_n + \sigma_s \frac{\Delta_n}{2} + (g_n - \delta g_n - \bar{g}_n + \sigma_s)\mu_B B, \quad (\text{C3})$$

with $E_v = 0$ and $E_c = E_g$. The expressions coincide with the monolayer ones, but with the new g -coefficient $g_n - \delta g_n + \bar{g}_n$. Moreover, the uk_\pm terms do not affect the odd states, and therefore such excitons have the same reduced masses as their monolayer analogs. Hence the corresponding trilayer exciton line has the same optoelectronic properties as it's monolayer analog. The odd A and B exciton transitions at the K^+ point are active only in σ^+ polarization. The corresponding energy shift in magnetic field is $\delta E_{A^o, B^o}^{\sigma^+} = [(g_c - \delta g_c) - (g_v - \delta g_v) - \bar{g}_c + \bar{g}_v]\mu_B B$. The same type of transitions at the K^- point are active in σ^- polarization and have the energy shift in magnetic field $\delta E_{A^o, B^o}^{\sigma^-} = -\delta E_{A^o, B^o}^{\sigma^+}$. It immediately gives us $g_{X_{A,B}^o} = 2(g_c - g_v) - 4\mathbf{g}$ for X_A^o and X_B^o exciton g -factors both for K^+ and K^- points of trilayer. Here we introduce the parameter

$$\mathbf{g} = \frac{1}{2}(\delta g_c + \bar{g}_c - \delta g_v - \bar{g}_v). \quad (\text{C4})$$

From the experiment we know that $g_{X_A^o} \approx -4.5$, which is close to monolayer $g_{X_A} = 2(g_c - g_v) \approx -4$. Therefore, we can roughly estimate $\mathbf{g} \approx 0.125$.

The second block is 2×2 matrix, written in the basis of even states $\{|\Upsilon_n^{(1)}\rangle \otimes |s\rangle, |\Upsilon_n^{(2)}\rangle \otimes |s\rangle\}$. Note that the structure of this matrix does not coincide with the structure of $G_n^{(2)}$. Therefore the subsystem of even states of trilayer demonstrates another behavior in magnetic field than it's bilayer analog. The conduction band states in

K^+ point are decoupled and have the energies

$$E_{cs}^{(1)} = E_g + \sigma_s \frac{\Delta_c}{2} + (g_c - \delta g_c + \bar{g}_c + \sigma_s - 2\sigma_s g_u) \mu_B B, \quad (C5)$$

$$E_{cs}^{(2)} = E_g - \sigma_s \frac{\Delta_c}{2} - (g_c - 2\delta g_c - \sigma_s - 2\sigma_s g_u) \mu_B B. \quad (C6)$$

The conduction band energies correspond to the states $\{|\Upsilon_c^{(1)}\rangle \otimes |s\rangle, |\Upsilon_c^{(2)}\rangle \otimes |s\rangle\}$. The valence band energies of admixed states as a function of magnetic field B are calculated similarly to the bilayer case.

The energy shifts of intralayer A and B excitons in σ^\pm polarizations at the K^+ point are $\delta E_{A,B}^{\sigma^\pm} = [\pm g_{A,B}^{(3)} + \mathbf{g}] \mu_B B$, where

$$g_A^{(3)} = -2g_u + \left(g_c - \frac{3}{2}\delta g_c + \frac{1}{2}\bar{g}_c\right) - \left(g_v - \frac{3}{2}\delta g_v + \frac{1}{2}\bar{g}_v\right) \frac{\Delta_v}{\sqrt{\Delta_v^2 + 8t^2}}, \quad (C7)$$

$$g_B^{(3)} = 2g_u + \left(g_c - \frac{3}{2}\delta g_c + \frac{1}{2}\bar{g}_c\right) - \left(g_v - \frac{3}{2}\delta g_v + \frac{1}{2}\bar{g}_v\right) \frac{\Delta_v}{\sqrt{\Delta_v^2 + 8t^2}}. \quad (C8)$$

The energy shifts for interlayer A' and B' excitons in both polarizations have the form $\delta E_{A',B'}^{\sigma^\pm} = [\pm g_{A',B'}^{(3)} + \mathbf{g}] \mu_B B$,

where

$$g_{A'}^{(3)} = 2g_u + \left(g_c - \frac{3}{2}\delta g_c + \frac{1}{2}\bar{g}_c\right) + \left(g_v - \frac{3}{2}\delta g_v + \frac{1}{2}\bar{g}_v\right) \frac{\Delta_v}{\sqrt{\Delta_v^2 + 8t^2}}, \quad (C9)$$

$$g_{B'}^{(3)} = -2g_u + \left(g_c - \frac{3}{2}\delta g_c + \frac{1}{2}\bar{g}_c\right) + \left(g_v - \frac{3}{2}\delta g_v + \frac{1}{2}\bar{g}_v\right) \frac{\Delta_v}{\sqrt{\Delta_v^2 + 8t^2}}. \quad (C10)$$

In the absence of \mathbf{g} the latter results coincide with the bilayer case up to redefinition of the parameters. The non-zero value of \mathbf{g} shows remarkable difference between pure bilayer and effective bilayer cases. The corresponding energy shifts in σ^\pm polarizations at the K^- point are $\delta E_{A,B}^{\sigma^\pm} = [\pm g_{A,B}^{(3)} - \mathbf{g}] \mu_B B$ and $\delta E_{A',B'}^{\sigma^\pm} = [\pm g_{A',B'}^{(3)} - \mathbf{g}] \mu_B B$.

This non-equivalency makes the analysis of the g -factors of the system more complicated. Let us consider the results of the measurements presented on the Fig. 8 more carefully, focusing mainly on X_A and X'_A exciton transitions. Again, according to the methodology of our experiment we measure the g -factor using the formula $g = [\delta E^{\sigma^+}(B) - \delta E^{\sigma^+}(-B)] / \mu_B B$. Then the g -factors at the K^+ point of intralayer X_A , X_B and interlayer X'_A , X'_B excitons are $g_{X_{A,B}}^{K^+} = 2g_{A,B}^{(3)} + 2\mathbf{g}$ and $g_{X'_{A',B'}}^{K^+} = 2g_{A',B'}^{(3)} + 2\mathbf{g}$ respectively. For K^- point transitions we obtain $g_{X_{A,B}}^{K^-} = 2g_{A,B}^{(3)} - 2\mathbf{g}$ and $g_{X'_{A',B'}}^{K^-} = 2g_{A',B'}^{(3)} - 2\mathbf{g}$. Taking into account the relative smallness of \mathbf{g} and absence of the results for magnetic field B larger than 14 T we suppose that the double g -factor structure of X_A and X'_A resonances is indistinguishable. Instead of this, probably, we observe only their average values $g_{X_{A,B}} = 2g_{A,B}^{(3)}$ and $g_{X'_{A',B'}} = 2g_{A',B'}^{(3)}$ respectively. One can mention that these average g -factors surprisingly coincide with the ones we can get from the standard formula $g = [E^{\sigma^+}(B) - E^{\sigma^-}(B)] / \mu_B B = [\delta E^{\sigma^+}(B) - \delta E^{\sigma^-}(B)] / \mu_B B$. The analysis of the signs of intra- and interlayer exciton g -factors can be done in the same way as in bilayer case.

[1] K. S. Novoselov, D. Jiang, F. Schedin, T. J. Booth, V. V. Khotkevich, S. V. Morozov, and A. K. Geim, *Two-dimensional atomic crystals*, Proc. Natl. Acad. Sci. U. S. A. **102**, 10451 (2005)

[2] Q. H. Wang, K.-Z. Kouros, A. Kis, J. N. Coleman, and M. S. Strano, *Electronics and optoelectronics of two-dimensional transition metal dichalcogenides*, Nat. Nanotech. **7**, 699 (2012)

[3] M. Koperski, M. R. Molas, A. Arora, K. Nogajewski, A. Slobodeniuk, C. Faugeras, and M. Potemski, *Optical properties of atomically thin transition metal dichalcogenides: Observations and puzzles*, Nanophotonics **6**, 1289 (2017)

[4] G. Wang, A. Chernikov, M. M. Glazov, T. F. Heinz, X. Marie, T. Amand, B. Urbaszek, *Excitons in atomically thin transition metal dichalcogenides*, Rev. Mod. Phys. **90**, 21001 (2018)

[5] K. F. Mak, C. Lee, J. Hone, J. Shan, and T. F. Heinz, *Atomically Thin MoS₂: A New Direct-Gap Semiconductor*, Phys. Rev. Lett. **105**, 136805 (2010)

[6] J. Binder, F. Withers, M. R. Molas, C. Faugeras, K. Nogajewski, K. Watanabe, T. Taniguchi, A. Kozikov, A. K. Geim, K. S. Novoselov, and M. Potemski, *Sub-bandgap voltage electroluminescence and magneto-oscillations in a WSe₂ light-emitting van der Waals heterostructure*, Nano Letters **17**, 1425 (2017)

- [7] C. Palacios-Berraquero, M. Barbone, D. M. Kara, X. Chen, I. Goykhman, D. Yoon, A. K. Ott, J. Beitner, K. Watanabe, T. Taniguchi, A. C. Ferrari, and M. Atatüre, *Atomically thin quantum light-emitting diodes*, Nat. Commun. **7**, 12978 (2016)
- [8] M. M. Ugeda, A. J. Bradley, S.-F. Shi, F. H. da Jornada, Y. Zhang, D. Y. Qiu, W. Ruan, S.-K. Mo, Z. Hussain, Z.-X. Shen, F. Wang, S. G. Louie, and M. F. Crommie, *Giant bandgap renormalization and excitonic effects in a monolayer transition metal dichalcogenide semiconductor*, Nat. Mater. **13**, 1091 (2014)
- [9] Z. Ye, T. Cao, K. O'Brien, H. Zhu, X. Yin, Y. Wang, S. G. Louie, and X. Zhang, *Probing excitonic dark states in single-layer tungsten disulphide*, Nature **513**, 214 (2014)
- [10] A. Chernikov, A. M. van der Zande, H. M. Hill, A. F. Rigosi, A. Velauthapillai, J. Hone, and T. F. Heinz, *Electrical Tuning of Exciton Binding Energies in Monolayer WS₂*, Phys. Rev. Lett. **115**, 126802 (2015)
- [11] A. V. Stier, N. P. Wilson, K. A. Velizhanin, J. Kono, X. Xu, and S. A. Crooker, *Magneto-optics of Exciton Rydberg States in a Monolayer Semiconductor*, Phys. Rev. Lett. **120**, 057405 (2018)
- [12] F. Withers, O. Del Pozo-Zamudio, A. Mishchenko, A. P. Rooney, A. Gholinia, K. Watanabe, T. Taniguchi, S. J. Haigh, A. K. Geim, A. I. Tartakovskii, and K. S. Novoselov, *Light-emitting diodes by band-structure engineering in van der Waals heterostructures*, Nat. Mater. **14**, 301 (2015)
- [13] F. Withers, O. Del Pozo-Zamudio, S. Schwarz, S. Duerwiel, P. M. Walker, T. Godde, A. P. Rooney, A. Gholinia, C. R. Woods, P. Blake, S. J. Haigh, K. Watanabe, T. Taniguchi, I. L. Aleiner, A. K. Geim, V. I. Fal'ko, A. I. Tartakovskii, and K. S. Novoselov, *WS₂ Light-Emitting Tunneling Transistors with Enhanced Brightness at Room Temperature* Nano Letters **15**, 8223 (2015)
- [14] G. Clark, J. R. Schaibley, J. Ross, T. Taniguchi, K. Watanabe, J. R. Hendrickson, S. Mou, W. Yao, and X. Xu, *Single Defect Light-Emitting Diode in a van der Waals Heterostructure*, Nano Letters **16**, 3944 (2016)
- [15] S. Schwarz, A. Kozikov, F. Withers, J. K. Maguire, A. P. Foster, S. Duerwiel, L. Hague, M. N. Makhonin, L. R. Wilson, A. K. Geim, K. S. Novoselov, and A. I. Tartakovskii, *Electrically pumped single-defect light emitters in WSe₂*, 2D Materials **3**, 025038 (2016)
- [16] S. M. Shinde, K. P. Dhakal, X. Chen, W. S. Yun, J. Lee, H. Kim and J.-H. Ahn, *Stacking-controllable interlayer coupling and symmetric configuration of multilayered MoS₂*, NPG Asia Materials, **10**, 468 (2018)
- [17] D. A. Ruiz-Tijerina, M. Danovich, C. Yelgel, V. Zólyomi, and Vladimir I. Fal'ko, *Hybrid $\mathbf{k} \cdot \mathbf{p}$ tight-binding model for subbands and infrared intersubband optics in few-layer films of transition-metal dichalcogenides: MoS₂, MoSe₂, WS₂, and WSe₂*, Phys. Rev. B **98**, 035411 (2018)
- [18] Y. Sun, D. Wang, and Z. Shuai, *Indirect-to-Direct Band Gap Crossover in Few-Layer Transition Metal Dichalcogenides: A Theoretical Prediction*, J. Phys. Chem. C **120** (38), 21866 (2016)
- [19] A. J. Bradley, M. M. Ugeda, F. H. da Jornada, D. Y. Qiu, W. Ruan, Y. Zhang, S. Wickenburg, A. Riss, J. Lu, S.-K. Mo, Z. Hussain, Z.-X. Shen, S. G. Louie, and M. F. Crommie, *Probing the Role of Interlayer Coupling and Coulomb Interactions on Electronic Structure in Few-Layer MoSe₂ Nanostructures*, Nano Lett. **15**(4), 2594 (2015)
- [20] S. Fang, R. K. Defo, S. N. Shirodkar, S. Lieu, G. A. Tritsarlis, and E. Kaxiras, *Ab initio tight-binding Hamiltonian for transition metal dichalcogenides*, Phys. Rev. B **92**, 205108 (2015)
- [21] T. Cheiwchanchamnangij and W. R. L. Lambrecht, *Quasiparticle band structure calculation of monolayer, bilayer, and bulk MoS₂*, Phys. Rev. B **85** 205302 (2012)
- [22] J. E. Padilha, H. Peelaers, A. Janotti, and C. G. Van de Walle *Nature and evolution of the band-edge states in MoS₂: From monolayer to bulk*, Phys. Rev. B **90**, 205420 (2014)
- [23] L. Debbichi, O. Eriksson, and S. Lebègue, *Electronic structure of two-dimensional transition metal dichalcogenide bilayers from ab initio theory*, Phys. Rev. B **89** 205311 (2014)
- [24] A. Splendiani, L. Sun, Y. Zhang, T. Li, J. Kim, C.-Y. Chim, G. Galli, and F. Wang, *Emerging Photoluminescence in Monolayer MoS₂*, Nano Lett. **10**, 1271 (2010)
- [25] A. Arora, M. Koperski, K. Nogajewski, J. Marcus, C. Faugeras, and M. Potemski, *Excitonic resonances in thin films of WSe₂: from monolayer to bulk material*, Nanoscale **7**, 10421 (2015)
- [26] A. Arora, K. Nogajewski, M. Molas, M. Koperski, and M. Potemski, *Exciton band structure in layered MoSe₂: from a monolayer to the bulk limit*, Nanoscale **7**, 20769 (2015)
- [27] M. R. Molas, K. Nogajewski, A. O. Slobodeniuk, J. Binder, M. Bartos, and M. Potemski, *Optical response of monolayer, few-layer and bulk tungsten disulfide*, Nanoscale **9**, 13128 (2017)
- [28] H. Zeng, G.-B. Liu, J. Dai, Y. Yan, B. Zhu, R. He, L. Xie, S. Xu, X. Chen, W. Yao and X. Cui, *Optical signature of symmetry variations and spin-valley coupling in atomically thin tungsten dichalcogenides*, Sci. Rep. **3**, 1608 (2013)
- [29] Y. Zhang, T.-R. Chang, B. Zhou, Y.-T. Cui, H. Yan, Z. Liu, F. Schmitt, J. Lee, R. Moore, Y. Chen, H. Lin, H.-T. Jeng, S.-K. Mo, Z. Hussain, A. Bansil and Z.-X. Shen, *Direct observation of the transition from indirect to direct bandgap in atomically thin epitaxial MoSe₂*, Nat. Nanotech. **9**, 111 (2014)
- [30] Z. Gong, G.-B. Liu, H. Yu, X. Cui, X. Xu, and W. Yao, *Magnetoelectric effects and valley-controlled spin quantum gates in transition metal dichalcogenide bilayers*, Nat. Commun. **4**, 2053, doi: 10.1038/ncomms3053 (2013)
- [31] Andor Kormányos, Viktor Zólyomi, Vladimir I. Fal'ko, and Guido Burkard, *Tunable Berry curvature and valley and spin Hall effect in bilayer MoS₂*, Phys. Rev. B **98**, 035408 (2018)
- [32] H.-P. Komsa and A. V. Krasheninnikov, *Electronic structures and optical properties of realistic transition metal dichalcogenide heterostructures from first principles*, Phys. Rev. B **88**, 085318 (2013)
- [33] M. Bernardi, M. Palummo, and J. C. Grossman, *Extraordinary Sunlight Absorption and One Nanometer Thick Photovoltaics Using Two-Dimensional Monolayer Materials*, Nano Lett. **13**, 3664 (2013)
- [34] S. B. Desai, G. Seol, J. S. Kang, H. Fang, C. Battaglia, R. Kapadia, J. W. Ager, J. Guo, and A. Javey, *Strain-Induced Indirect to Direct Bandgap Transition in Multilayer WSe₂*, Nano Lett. **14**, 4592(2014)
- [35] K. P. Dhakal, D. L. Duong, J. Lee, H. Nam, M. Kim, M.

- Kan, Y. H. Lee and J. Kim, *Confocal absorption spectral imaging of MoS₂: optical transitions depending on the atomic thickness of intrinsic and chemically doped MoS₂*, *Nanoscale* **6**, 13028 (2014)
- [36] W. Zhao, Z. Ghorannevis, L. Chu, M. Toh, C. Kloc, P.-H. Tan, and G. Eda, *Evolution of Electronic Structure in Atomically Thin Sheets of WS₂ and WSe₂*, *ACS Nano* **7**, 791 (2013)
- [37] A. Arora, M. Koperski, A. O. Slobodeniuk, K. Nogajewski, R. Schmidt, R. Schneider, M. R. Molas, S. Michaelis de Vasconcellos, R. Bratschitsch, M. Potemski, *Zeeman spectroscopy of excitons and hybridization of electronic states in few-layer WSe₂, MoSe₂ and MoTe₂*, in preparation
- [38] J. Horng, T. Stroucken, L. Zhang, E. Y. Paik, H. Deng, and S. W. Koch, *Observation of interlayer excitons in MoSe₂ single crystals*, *Phys. Rev. B* **97**, 241404(R) (2018)
- [39] A. Arora, M. Drüppel, R. Schmidt, T. Deilmann, R. Schneider, M. R. Molas, P. Marauhn, S. Michaelis de Vasconcellos, M. Potemski, M. Rohlfing, and R. Bratschitsch, *Interlayer excitons in a bulk van der Waals semiconductor*, *Nat. Commun.* **8**, 639 (2017)
- [40] J. Wierzbowski, J. Klein, F. Sigger, C. Straubinger, M. Kremser, T. Taniguchi, K. Watanabe, U. Wurstbauer, A. W. Holleitner, M. Kaniber, K. Müller, and J. J. Finley, *Direct exciton emission from atomically thin transition metal dichalcogenide heterostructures near the lifetime limit*, *Sci. Rep.* **7**, 12383 (2017)
- [41] G. Wang, C. Robert, M. M. Glazov, F. Cadiz, E. Courtade, T. Amand, D. Lagarde, T. Taniguchi, K. Watanabe, B. Urbaszek, and X. Marie, *In-Plane Propagation of Light in Transition Metal Dichalcogenide Monolayers: Optical Selection Rules*, *Phys. Rev. Lett.* **119**, 047401 (2017)
- [42] D. Vaclavkova, J. Wyzula, K. Nogajewski, M. Bartos, A. O. Slobodeniuk, C. Faugeras, M. Potemski, and M. R. Molas, *Singlet and triplet trions in WS₂ monolayer encapsulated in hexagonal boron nitride*, *Nanotechnology* **29**, 325705 (2018)
- [43] S.-Y. Chen, T. Goldstein, J. Tong, T. Taniguchi, K. Watanabe, and J. Yan, *Superior Valley Polarization and Coherence of 2s Excitons in Monolayer WSe₂*, *Phys. Rev. Lett.* **120**, 046402 (2018)
- [44] F. Cadiz, E. Courtade, C. Robert, G. Wang, Y. Shen, H. Cai, T. Taniguchi, K. Watanabe, H. Carrere, D. Lagarde, M. Manca, T. Amand, P. Renucci, S. Tongay, X. Marie, and B. Urbaszek, *Excitonic Linewidth Approaching the Homogeneous Limit in MoS₂ - Based van der Waals Heterostructures*, *Phys. Rev. X* **7**, 021026 (2017)
- [45] G.-B. Liu, D. Xiao, Y. Yao, X. Xu, and W. Yao, *Electronic structures and theoretical modelling of two-dimensional group-VIB transition metal dichalcogenides*, *Chem. Soc. Rev.* **44**, 2643 (2015)
- [46] A. Kormányos, G. Burkard, M. Gmitra, J. Fabian, V. Zólyomi, N. D. Drummond, and V. Fal'ko, *k · p theory for two-dimensional transition metal dichalcogenide semiconductors*, *2D Materials* **2**, 022001 (2015)
- [47] H. Terrones, F. López-Uras, and M. Terrones, *Novel hetero-layered materials with tunable direct band gaps by sandwiching different metal disulfides and diselenides*, *Sci. Rep.* **3**, 1549 (2013)
- [48] A. Castellanos-Gomez, M. Buscema, R. Molenaar, V. Singh, L. Janssen, H. S. J. van der Zant, and G. A. Steele, *Deterministic transfer of two-dimensional materials by all-dry viscoelastic stamping*, *2D Materials* **1**, 011002 (2014)
- [49] T. Taniguchi and K. Watanabe, *Synthesis of high-purity boron nitride single crystals under high pressure by using Ba BN solvent* *J. Cryst. Growth* **303**, 525 (2007)
- [50] M. Koperski, M. R. Molas, A. Arora, K. Nogajewski, M. Bartos, D. Vaclavkova, J. Wyzula, and M. Potemski, *Orbital, spin and valley contributions to Zeeman splitting of excitonic resonances in MoSe₂, WSe₂ and WS₂ monolayers*, *2D Materials*, doi: 10.1088/2053-1583/aae14b (2018), arXiv:1803.00376 [cond-mat.mtrl-sci]
- [51] C. Robert, M. A. Semina, F. Cadiz, M. Manca, E. Courtade, T. Taniguchi, K. Watanabe, H. Cai, S. Tongay, B. Lassagne, P. Renucci, T. Amand, X. Marie, M. M. Glazov, and B. Urbaszek, *Optical spectroscopy of excited exciton states in MoS₂ monolayers in van der Waals heterostructures*, *Phys. Rev. Materials* **2**, 011001(R) (2018)
- [52] A. A. Mitioglu, K. Galkowski, A. Surrente, L. Klopptowski, D. Dumcenco, A. Kis, D. K. Maude, and P. Plochocka, *Magnetoexcitons in large area CVD-grown monolayer MoS₂ and MoSe₂ on sapphire*, *Phys. Rev. B* **93**, 165412 (2016)
- [53] A. V. Stier, K. M. McCreary, B. T. Jonker, J. Kono, and S. A. Crooker, *Exciton diamagnetic shifts and valley Zeeman effects in monolayer WS₂ and MoS₂ to 65 Tesla*, *Nat. Comm.* **7**, 10643 (2016)
- [54] Y. J. Wu, C. Shen, Q. H. Tan, J. Shi, X. F. Liu, Z. H. Wu, J. Zhang, P. H. Tan, and H. Z. Zheng, *Valley Zeeman splitting of monolayer MoS₂ probed by low-field magnetic circular dichroism spectroscopy at room temperature*, *Appl. Phys. Lett.* **112**, 153105 (2018)
- [55] R. Pisoni, A. Kormányos, M. Brooks, Z. Lei, P. Back, M. Eich, H. Overweg, Y. Lee, P. Rickhaus, K. Watanabe, T. Taniguchi, A. Imamoglu, G. Burkard, T. Ihn, K. Ensslin, *Interactions and magnetotransport through spin-valley coupled Landau levels in monolayer MoS₂*, arXiv:1806.06402v1 (2018)
- [56] N. Wakabayashi, H. G. Smith, and R. M. Nicklow, *Lattice dynamics of hexagonal MoS₂ studied by neutron scattering* *Phys. Rev. B* **12**, 659 (1975)